

4D Printing of Programmable Digital Metamaterials

Ido Levin^{1,2}, Ela Sachyani³, Rama Lieberman³, Noa Battat³, Eran Sharon¹, Shlomo Magdassi³

Abstract

Modern 3D printers allow for the accurate placing of microscopic material voxels, to form complex three-dimensional structures. The advancing capabilities in multi-material printing, coupled with the discovery of printable responsive materials, pave the way for the 3D printing of digital materials, and for the 3D printing of shape-transforming structures, or 4D printing. In this work, we leverage and combine these advancements to develop a versatile methodology for crafting digitized 4D-printed shape-transforming sheets. We 3D print digital responsive sheets, composed of active and passive voxels that are meticulously positioned to form thin structures that can be actuated on demand. This methodology enables us to encode the lateral geometry and the reference curvature, separately and simultaneously. Our approach grants us comprehensive control over the resulting shape, unlocking novel opportunities in synthetic shape-morphing materials. Furthermore, it has the potential to program anomalous mechanical properties and to be extended to multi-material and metamaterial systems.

Introduction

Swelling-induced morphological changes of elastic sheets are ubiquitous across many length scales^{1–3} and inspired many multidisciplinary endeavors. Often, the emerging shape is achieved via *differential swelling* – a non-uniform swelling of the sheet. There, the shape is controlled only by the local information encoded within the swelling magnitude and/or orientation at different locations. In the past decade, this concept was realized in several man-made structures, primarily by introducing gradients in the deformation across the thickness, resulting in a programmed reference curvature^{4–6}. A parallel approach used lateral gradients in the deformation to prescribe Gaussian curvature^{7–10}. These structures were shown to have rich configurational phase space and the capability to generate complex patterns by breaking the symmetry of the underlying fields. However, up to date, the ability to determine a desired three-dimensional (3D) shape is still only partial. To achieve complete control over the shape, one must be able to accurately impose swelling gradients both laterally and across the thickness, a task that has not been achieved yet.

Experimentally, the principal strategy to induce differential swelling is by using responsive materials. These include hydrogels^{7,10–12}, nematic elastomers^{8,9}, and dielectric elastomers¹³. Choosing the right material involves taking into account both the material properties and the method to program differential swelling. Hydrogels are advantageous as they can be responsive to a variety of external triggers such as temperature, pH, light, and humidity^{14,15}, and can be repeatedly actuated. The response can be tailored to yield a relative volumetric shrinkage as high as 100-fold¹⁶ and objects made of hydrogels are suitable for integration in the field of soft robotics, implants, and drug delivery^{17–19}. Recently, there has been a growing interest in hydrogel-made objects, including fabrication by 3D printing^{20–25}. Among the available 3D printing technologies, direct ink writing (DIW) and stereolithography (SLA), including digital light processing (DLP), are the most used for printing hydrogels.

1 Racah Institute of Physics, The Hebrew University, Jerusalem 91904, Israel

2 Department of Chemistry, University of Washington, Seattle, WA 98195

3 Institute of Chemistry, The Hebrew University of Jerusalem, Jerusalem 9190401, Israel

Hydrogels also provide several techniques for accurate control of the swelling field. Lithography-like approaches allow very high spatial resolution^{10,26}. Alternatively, shear alignment can be utilized to control the orientation of rigid fibers inside printed gel sheets, resulting in anisotropic swelling²⁷. Some of these systems also enable limited gradients in the thin dimension by asymmetric polymerization²⁸ or by combining two different layers²⁹. However, optimal three-dimensional control over the deformation field, which would enable free programming of shapes, has not yet been achieved.

Theoretically, the shaping of thin sheets via differential swelling was formulated in the theory of non-Euclidean elasticity³⁰. In this formalism, every swelling field induces a reference geometry, which is expressed by the *reference metric*, $\bar{\mathbf{a}}$, which results from lateral gradients of the swelling field, and the *reference curvature*, $\bar{\mathbf{b}}$, which results from variations of swelling across the thickness. Shape selection (i.e., choosing an *actual metric*, \mathbf{a} , and an *actual curvature*, \mathbf{b}) is done by minimizing the elastic energy

$$(1) E = \int t(\mathbf{a} - \bar{\mathbf{a}})^2 + t^3(\mathbf{b} - \bar{\mathbf{b}})^2$$

The first term is the stretching energy. It is linear in the sheet's thickness, t , and depends on the lateral elastic strain, which is expressed as the difference between the actual and reference metrics. The second term, bending, is cubic in t and depends on the difference between the actual and reference curvature. In many cases $\bar{\mathbf{a}}$ and $\bar{\mathbf{b}}$ are incompatible; that is, no surface can simultaneously satisfy both $\mathbf{a} = \bar{\mathbf{a}}$, and $\mathbf{b} = \bar{\mathbf{b}}$. In such cases, the shape is determined by a competition between bending and stretching. This competition is the source for many of the rich phenomena observed in such systems: shape transitions⁴, breaking of symmetry^{31,32}, and fractal structures^{33,34}.

For very thin sheets, the stretching energy becomes dominant (due to the different exponents of t in the two energy terms), hence the configuration will be an approximate embedding of the reference metric (i.e., $\mathbf{a} = \bar{\mathbf{a}}$). Therefore, an apparent design strategy for shaping is to program $\bar{\mathbf{a}}$ that is identical to the metric of the desired surface, a task that can be done analytically¹⁰ or numerically³⁵. However, finding the metric is not enough as there usually are many different embeddings (i.e., surfaces with that metric), and therefore guiding the shape selection using $\bar{\mathbf{b}}$, *in addition* to $\bar{\mathbf{a}}$, is crucial¹². For instance, inducing the reference metric corresponding to a spherical cap will result in a bi-stable structure that can buckle in both directions. A reference curvature must be determined in addition, to assure buckling upwards into a dome or downwards, into a cap. Indeed, the impressive control over $\bar{\mathbf{a}}$ presented in¹² and³⁶ could guarantee desired 3D shapes only in a limited range of cases. Moreover, when the sheet is not infinitely thin, finite thickness effects appear, shifting \mathbf{a} away from $\bar{\mathbf{a}}$. Finally, beyond full control over shaping, the ability to simultaneously control both $\bar{\mathbf{a}}$ and $\bar{\mathbf{b}}$, could open the way for programming exotic mechanical properties into elastic sheets³⁷⁻³⁹.

In this work, we present a novel 3D printing strategy for fabricating hydrogel sheets with a digitized reference geometry, enabling control over both $\bar{\mathbf{a}}$, and $\bar{\mathbf{b}}$. As such, it enables fabricating smart materials with a broad range of programmed 3D shapes and controlled mechanical properties. Furthermore, it provides a design and simple process to fabricate multi-material structures via pixelization. We fabricate bi-material composite structures by a common SLA 3D printer, based on printing two different materials with localized crosslinking, which are composed of voxels of polyacrylic acid with polyethylene glycol diacrylate (PEGDA) as a crosslinker. The 3D printing of gels with two crosslinking densities enables the printing of voxels that swell by different ratios upon hydration. The relative spatial concentration of the printed voxels of each type determines the magnitude of the local swelling. Therefore, in a coarse-grained

view, it enables programming continuous three-dimensional swelling fields. We repeat this process for two layers, resulting in high-resolution digital 4D structures with a swelling factor that can be programmed and controlled in 3D, thus locally determining both \bar{a} , and \bar{b} .

Results

The new approach is based on three stages: 1. *Design*, in which the smooth swelling field is calculated. 2. *Pixelization*, in which the smooth field is digitized into the desired resolution. 3. *Fabrication*, in which the desired flat structure is 3D printed (Fig. 1). Then, the programmed geometry is *actuated* by hydrating the gel in water.

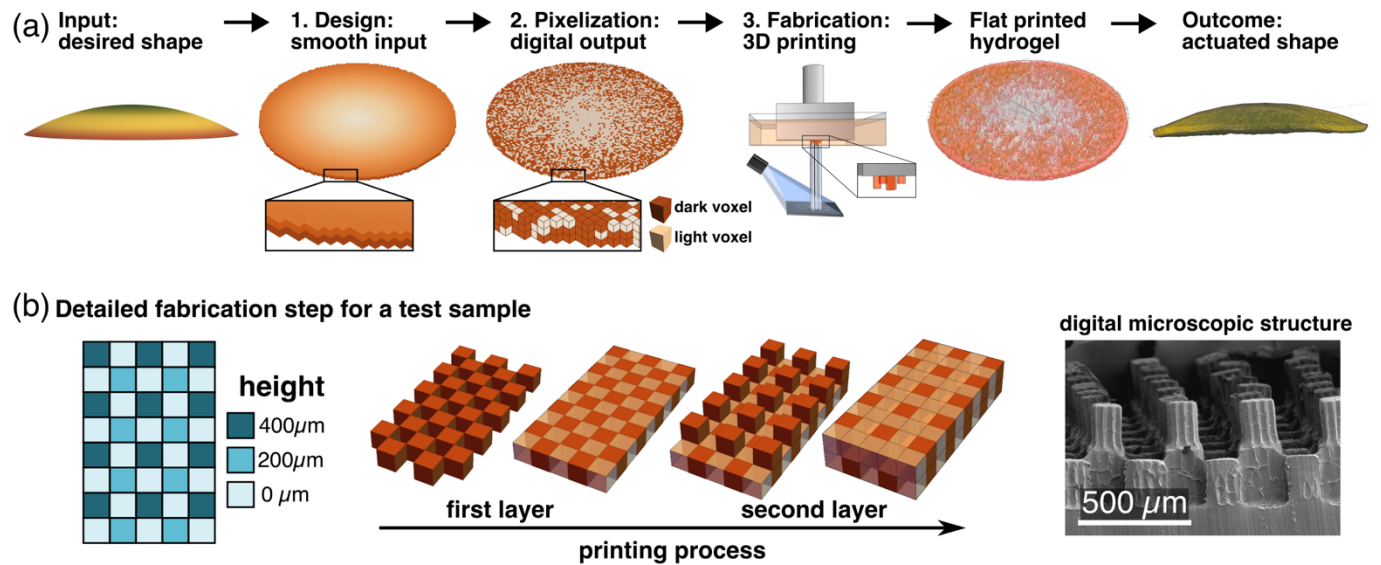


Figure 1. Design, Digitization, and Fabrication. (a) Outline of our technique: The geometry of the desired shape is analyzed, resulting in its metric and curvature fields. The analysis results in a smooth conformal swelling density field for each layer(1). The two smooth density fields are digitized(2). The digitized geometry is realized by multi-material 3D printing(3). The resulting flat sample is actuated in water forming the desired 3D shape. (b) Detailed Illustration of the fabrication step. A test voxelated structure consisting of pillars made of dark voxels of 2 heights: 200 μm (a single voxel) and 400 μm (two stacked voxels). (left). Steps of the multi-material printing (center). SEM image of the printed structure (here, only the dark voxels were printed for visualization; right).

While the approach has the potential to print fully 3D structures, here we focus on printing thin structures with only two layers (bilayers), as a proof of concept. These are sufficiently complex to allow simultaneous control over both \bar{a} and \bar{b} . The discrete nature of the voxelated structure, while smoothed by the elastic response of the material, yields an effective smooth reference geometry. Therefore, an important quantity is the ratio between the thickness and the spatial resolution of the voxels. This ratio must be large enough, i.e., the voxel size must be small compared to the thickness (similar to how black and white pixels are converted into a grayscale image when the resolution is sufficiently high; see a related scenario in ¹⁰). We print our material on a discrete Cartesian grid, such that every printed voxel is composed of either low or high crosslinking density gels (Fig. 1a). To verify that our printing resolution is high enough to fabricate discrete structures we print a test sample composed only of dark voxels and scan it in SEM(Fig.

1b). In this case, each layer has a programmed effective coarse-grained density field, $\rho(x, y)$, defined as the density of the denser voxels. As a result, an associated isotropic swelling field $\omega(x, y)$ is prescribed for each layer independently. The constitutive relation, $\omega(\rho)$, depends on the material properties and determines the mechanical response to the voxel density field.

Denoting the swelling field at the top and bottom layers, ω_t , and ω_b , respectively, the resulting non-Euclidean reference tensors read (see supplementary information for details):

$$(2) \bar{\mathbf{a}} = \frac{1}{4}(\omega_t + \omega_b)^2 \begin{pmatrix} 1 & 0 \\ 0 & 1 \end{pmatrix}, \bar{\mathbf{b}} = \frac{3}{t} \begin{pmatrix} \omega_t - \omega_b \\ \omega_t + \omega_b \end{pmatrix} \begin{pmatrix} 1 & 0 \\ 0 & 1 \end{pmatrix}$$

Note that while an isotropic swelling provides full control over, $\bar{\mathbf{a}}$, (i.e., any reference metric can be realized), it can only prescribe isotropic curvatures. Nevertheless, it provides control over the *direction* of curvature, which is impossible by prescribing only $\bar{\mathbf{a}}$.

There are many different inverse-design heuristics, but since the printed sheets are thin, their configurations must be very close to the isometric embedding of the reference metric, $\bar{\mathbf{a}}$ (see Eq. 1). This implies that to obtain the desired configuration with some metric \mathbf{a} , ω_t and ω_b must be properly selected to have $\bar{\mathbf{a}} \approx \mathbf{a}$. By that, we also overcome the limitation of our ability to control $\bar{\mathbf{b}}$, as $\bar{\mathbf{a}}$ induces the Gaussian curvature, and $\bar{\mathbf{b}}$ controls the mean curvature (by biasing the direction of curvature). Therefore, we start by computing the metric first and then adding the curvature to each layer. In this case, it is more natural to express Eq. 2 using the *metric generator* (average swelling), $\omega_0 \equiv \frac{1}{2}(\omega_t + \omega_b)$, and the *curvature generator* (swelling variation) $\Delta \equiv \omega_t - \omega_b$, which reads:

$$(3) \bar{\mathbf{a}} = \omega_0^2 \begin{pmatrix} 1 & 0 \\ 0 & 1 \end{pmatrix}, \bar{\mathbf{b}} = \frac{3\Delta}{2t\omega_0} \begin{pmatrix} 1 & 0 \\ 0 & 1 \end{pmatrix}$$

For simple cases, the reference metric can be analytically calculated directly from the desired shape. For more complex shapes, one can use numerical methods such as the Boundary First Flattening (BFF) algorithm that finds conformal parameterization of desired surfaces³⁵. That is, finding a mapping of the curved surface into a plane that does not distort angles but is allowed to swell/compress different sections (Fig. 1 a). As such, the algorithm provides us with the optimal ω_0^2 field on a flat domain, i.e., fully determines $\bar{\mathbf{a}}$. We are still left with the freedom of selecting Δ , to prescribe the desired $\bar{\mathbf{b}}$.

Each printed layer is formed as follows: voxels of the first material are printed, the bath is replaced, and then a layer of the second material is printed (Fig. 1b). For visualization purposes, we color orange the voxels made of the gel with the higher crosslinking ratio. The colored and uncolored voxels are referred to as “*dark*”, and “*light*” voxels, respectively. This method is advantageous to molding the second material as it provides better control and flexibility and provides support for the next layer. Moreover, it can be generalized to an arbitrary number of consecutive materials. In the present case, this process is repeated twice, forming a bi-material composite structure with the desired properties. Benefiting from the high resolution of typical commercial DLP printers, we can make sure that the digitization is made in a length scale that is smoothed by elasticity, reproducing the original continuous field. The result is a smart material, that when immersed in water, swells into the programmed shape.

Calibration

To calibrate our system, we must first find the constitutive relation, $\omega(\rho)$, where ρ is the density of the dark voxels. To achieve this, we print calibration objects made of a single layer with a uniform dark-voxel density (0% to 40%). The printed objects are immersed in water for swelling, up to their final size. When completely swollen, we measure the relative change in their length, $\omega = \frac{\ell}{\ell_0}$, where ℓ and ℓ_0 are the swollen and original lengths, respectively. As expected, the lengthening is reduced as the density of the dark voxels is increased. The resulting constitutive law is almost linear in the pillar density and presents a 25% relative longitudinal swelling between the extremal densities (Fig. 2a). The fact that the swollen object remains flat and isotropic, suggests that the printing resolution is sufficiently high so that the discrete reference geometry is smoothed by elasticity. This measurement enabled calibrating the emerging reference metric, hence, to inverse-design density profiles for desired shapes of plates in the thin limit, either analytically, or by using the BFF algorithm.

Next, we construct sheets with uniform ω_0 (hence the lateral geometry is Euclidean), while controlling the reference curvature by prescribing gradients in the thin dimension (controlling Δ). This ability is crucial for the selection of a desired configuration among all isometries of the reference metric. We print structures with a uniform voxel density on either the top or the bottom layer, with the other layer empty (composed entirely of light voxels). Upon actuation, the swelling gradient results in curvature that can be predicted by substituting the constitutive law into Eq. 3. The predicted magnitudes of the emerging curvatures match all the measurements very well, with no fitting parameters (Fig. 2b), and we demonstrate the ability to control the curvature in both directions (curving upwards and downwards).

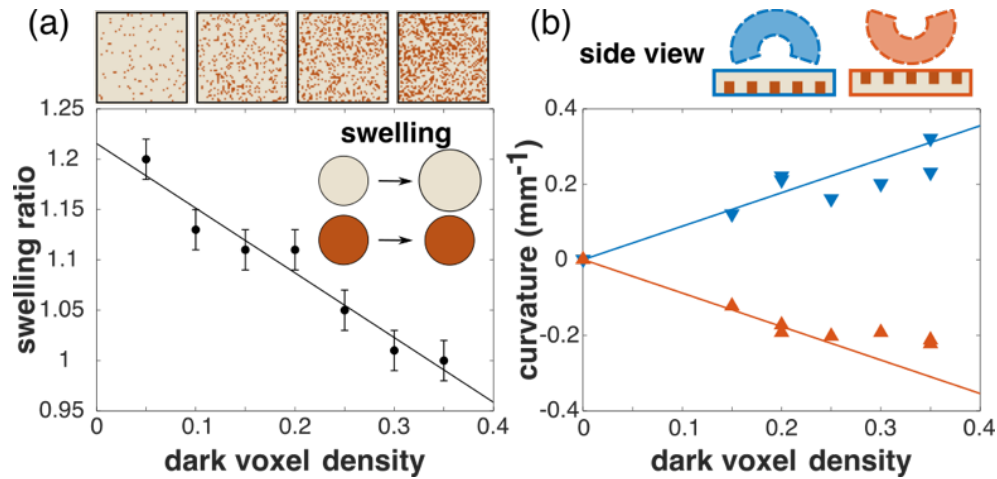


Figure 2.. *Calibration measurement of longitudinal elongation and curvature.* (a) The longitudinal swelling ratio (the ratio between the actuated and original lengths) of calibration samples with a uniform voxel density (dark circles). The fitted linear trend (black line) suggests a monotonic dependence of the swelling factor, ω , on the pillar concentration. Relative swelling of almost 25% was achieved, allowing significant freedom in prescribing shapes. The variation in the discrete geometry is illustrated in the squares above. (b) The prescribed curvature for specimens with one layer with a uniform voxel density and the other with no dark voxels at all (red and blue points, corresponding to dark voxels only on top or bottom, respectively). The solid lines result directly from plugging the swelling calibration fit in (a) into Eq.3 (i.e., there are no fitting parameters). These results demonstrate the capability to prescribe curvature in either direction and allow us to program the reference fields quantitatively.

Introducing lateral density gradients

Once the constitutive law is known, we introduce spatial gradients to the pillar densities in order to program more complicated shapes. We start with simple examples where $\Delta = 0$ (hence, $\bar{\mathbf{b}} = 0$), and the spatial variations are linear ($\omega_0(r, \theta) = \alpha r + \beta$). Such profiles, with increasing/decreasing trends, prescribe Gaussian curvature with a negative/positive sign (i.e., dome-like/saddle-like), respectively. By this approach, we demonstrate the formation of 3D shapes that are governed by radial changes, such as dome-like and combined, dome-saddle-like structures (Fig. 3). The control over the shape is not just qualitative: We calculate and print the fields needed for spherical caps with different radii in the range 0.5-2 cm (see Supplementary Material). The gels morph into caps with the prescribed spherical angle and radius (Fig. 3 (c)).

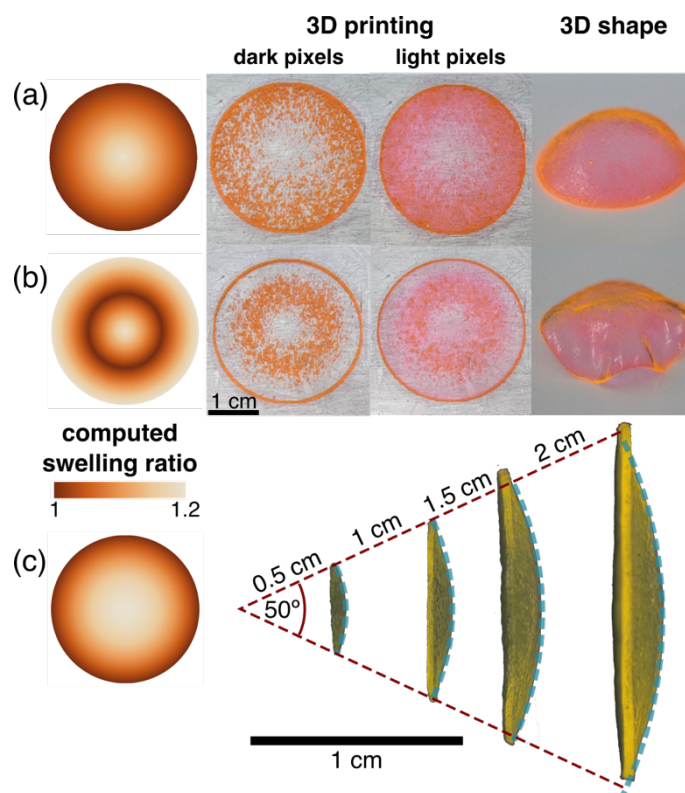


Figure 3. Control of lateral swelling gradients (a-b) Basic samples with axisymmetric swelling gradients, either increasing monotonically (a, left panel), or increasing and then decreasing (b, left panel). This results in a spherical structure, or a spherical center with wavy rims (right panels of a, b, respectively). (c) Printed gels with a swelling field corresponding to the metric of a sphere. We printed four samples of different sizes with reference metrics of spheres with varying radii in the range of 0.5-2 cm and a fixed spherical angle of 50° (dashed teal arcs). The swollen gels adopt these configurations as illustrated by the tight fit of the arcs.

Next, we test the ability to introduce spatial gradients in the induced reference curvature by 3D printing disks with uniform average pillar densities (hence $\bar{\mathbf{a}}$ is flat), which varies sinusoidally between the two layers as a function of the azimuthal angle, as shown in Fig. 4. In this case, the reference curvature sign oscillates, thus bending the disk up and down. We design and print such structures with 3,4,5 and 6 nodes. The emerging shapes indeed follow the prescribed number of nodes, indicating that we can spatially

control the direction of curvature. Note that this shape has very little Gaussian curvature (the curvature is mostly uniaxial, oriented in the azimuthal direction). As such, the direction of the curvature is induced while the stretching energy associated with these structures remains small.

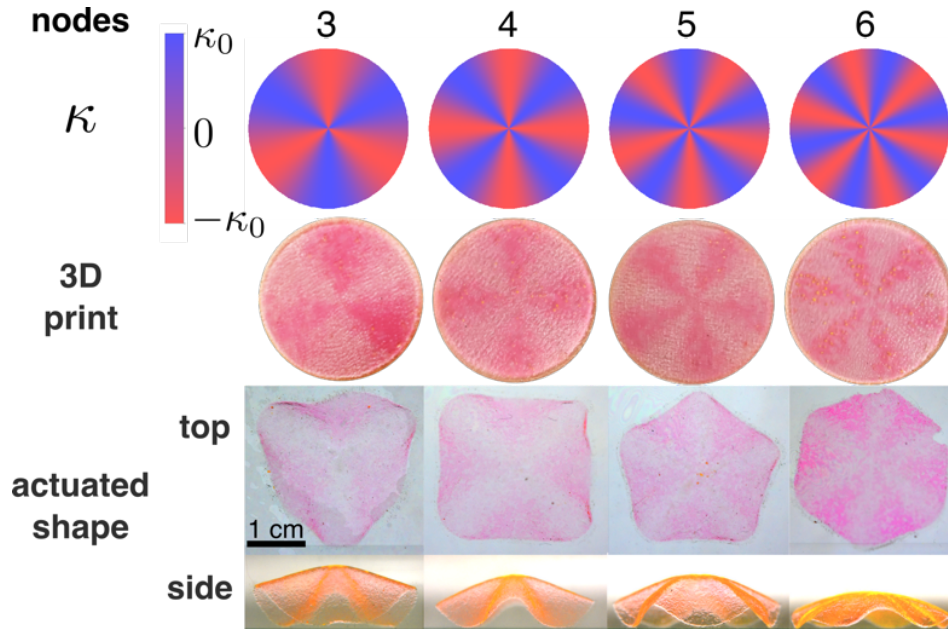


Figure 4. Discs with an azimuthally oscillating reference curvature and a flat reference metric. We print structures with a varying number of nodes (3,4,5, and 6), demonstrating our ability to induce shape by controlling the spatial distribution of the reference curvature. All samples are circular. The apparent polygonal contour (third row) results solely from 3D projection effects.

Finally, once our ability to separately control \bar{a} and \bar{b} is established, we focus on controlling them simultaneously. To demonstrate the effect of both fields, we design a model composed of two spherical caps with a small overlap (Fig. 5). Each cap has the same swelling factor of a spherical cap used in Fig. 3 (c) (i.e., the same ω_0 field), but a different sign of the reference curvature (i.e., the opposite Δ field). The magnitude of the reference curvature is designed to match the radius of curvature of the sphere, and its sign changes from positive in the left half to negative in the right half (\bar{b} vanishes in the overlap region). These two conditions determine ω_0 and Δ , and hence the entire design. All printed structures robustly morphed into the designed double-dome shape, with a positive and negative mean curvature in the domes. The radius of curvature of each half matches quantitatively the programmed one (Fig. 5 (d)). These results display the advantage of our method, as it is absolutely impossible to get this configuration by controlling only one of the two reference fields.

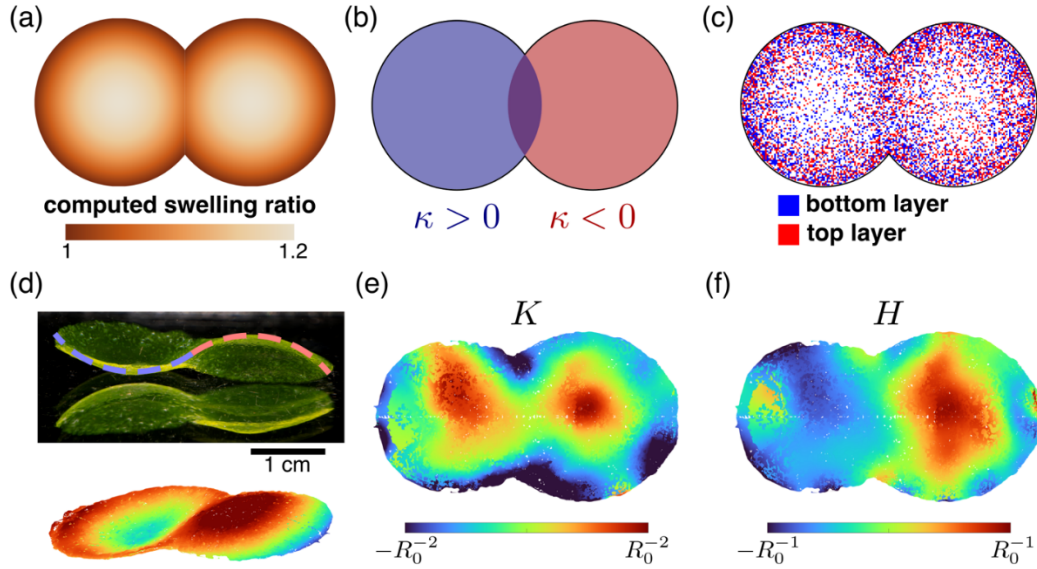


Figure 5. **A simultaneous control over the reference metric and curvature.** We design and print a structure composed of two identical spherical caps, each with a different reference curvature direction (final radius: 15 mm, printed radius: 11 mm, overlap 4.4 mm) (a) The reference metric is the same for both halves and is identical to the one on Fig. 3. (c) The reference curvature is uniform in each half and is identical in magnitude to the one encoded in the reference metric but have opposite signs. (c) The resulting voxel map, where color indicates the layer of each dark voxel (blue – top layer, red – bottom layer). (d) The swollen sample (and its reflection) demonstrates our ability to control both reference fields together (top). The dashed line corresponds to the programmed radius of curvature, illustrating the quantitative agreement with the designed configuration. The sample is 3D scanned and smoothed (bottom). The calculated Gaussian and mean curvatures, (e) and (f), respectively, illustrate the double dome structure

Conclusions

This work suggests a novel strategy based on 3D printing to design and fabricate self-morphing sheets of smart materials with programmed responsive geometry. Until now, experimental realizations of self-morphing were limited to control over *either* a reference metric or a reference curvature fields and, therefore, had only partial control over the configuration. Here, we go beyond the state of the art by developing a method for simultaneously determining both fields, which, together, *determine* the reference geometry. In our approach, the 3D printer is not used to build a 3D structure explicitly. Instead, we use its high resolution and accuracy to encode digital information into a thin, flat sample. Upon actuation, this information drives the self-morphing of the sheet into the desired, accurately predicted 3D shape. This strategy, i.e., of using a printer as a programming machine, the digitization and the separation to lateral and vertical gradients are applicable with other responsive materials, suggests a new approach to self-morphing. In this work, we limited the study to isotropic swelling, which provides control over the direction of curvature. We suggest that by introducing x-shaped elements (rather than circular pillars), one can induce effective anisotropy to the curvature. Moreover, there is a strong desire for a shape-morphing structure that can operate under orthogonal actuation modes (such as temperature and pH), which, using traditional fabrication techniques, is not straightforward⁴⁰. However, with our system, achieving this merely entails printing voxels composed of various responsive materials with the required actuation modes.

Combining computation of the swelling field needed for obtaining a desired 3D shape with pixelization, makes our approach compatible with all common 3D printers based on stereolithography processes, allowing one to print the structure using only two materials, thus simplifying the fabrication process. The ability to control both the metric and the curvature opens new directions for 4D designs. 3D structures can be made fully compatible (i.e., have a compatible reference metric and curvature) and thus have a single, well-defined equilibrium shape, but can also be made weakly or strongly incompatible. As the degree of incompatibility increases, the resultant structures could have many meta-stable configurations, and the structures would become more responsive mechanically. We note that beyond the ability to specify a desired 3D shape, the ability to accurately control both metric and curvature can be used to fabricate structures with exotic mechanical properties, significantly expanding the notion of "smart materials".

Materials and Methods

Acrylic acid was purchased from Acros (Belgium). TPO photo-initiator diphenyl(2,4,6-trimethylbenzoyl)phosphine oxide was obtained from BASF (Germany). The surfactant SDS, Sodium Dodecyl Sulfate, and dye Rhodamine 6G were purchased from Sigma Aldrich (Merck, Germany). PEGDA was obtained as a gift from Sartomer-Arkema (France). Triple distilled water (TDW) was obtained from NANOpure[®]-DiamondTM (TDW; 0.0055 $\mu\text{S}\cdot\text{cm}^{-1}$; Barnsted system, IA, USA).

Digitization of the concentration fields: Once the desired \bar{a} and \bar{b} are calculated, we extract the metric and curvature generators, ω_0 , and Δ , and then calculate the smooth density field of each layer. Then, each voxel is assigned a material independently according to the local density value. For instance, if the local density value is 0.2, the probability that it will be assigned a dark or a light voxel, is 20% and 80%, respectively.

Printing formulation: The printing compositions are based on materials previously developed in our lab²¹. Two types of UV-curable aqueous solutions inks containing acrylic acid with polyethylene glycol diacrylate (PEGDA) as a crosslinker were prepared: one with low wt% of PEGDA (2wt% PEGDA, 38wt% acrylic acid, TDW 58wt%) and another with high wt% of PEGDA (6wt% PEGDA, 34wt% acrylic acid, TDW 58 wt%). For both printing compositions, 2wt% of the photoinitiator, Diphenyl(2,4,6-trimethylbenzoyl)phosphine oxide (TPO) in the form of water dispersible nanoparticles were added (with ionic SDS as a surfactant). All the materials were stirred together until the photoinitiator powder was fully dispersed and a clear solution was obtained. Rhodamine 6G was added as a dye to the solution with a high wt% of PEGDA, to distinguish between the solutions.

Multi-material 3D printing: The inks were printed with a DLP printer (Pico2, Asiga, Australia) with a 385nm UV-LED light source. Each printed layer's thickness was 200 μm , with a light intensity of 25 mW/cm^2 and exposure times of 3 and 4 seconds, for the high and low PEGDA wt%, respectively. The dual-material printing was utilized by pausing the printing and switching the baths. In total, three bath replacements were conducted to form two multi-material layers.

Authors contribution

I.L., E.Sh, and S.M. designed the research. I.L. designed the printed structures. E.Sa., R.L., and N.B. printed the hydrogel sheets. I.L. measured the induced shape transformations. I.L., E.Sa, E.Sh, and S.M. wrote the manuscript and produced the figures. I.L. and E.Sa have equally contributed to this work. E.Sh. and S.M. have jointly supervised the work.

Data availability

The data that support the findings of this study are available from the corresponding author upon request.

Competing interests

The authors declare no competing interests.

References

1. Yoneda, M., Kobayakawa, Y., Kubota, H. Y. & Sakai, M. Surface contraction waves in amphibian eggs. *J Cell Sci* **54**, 35–46 (1982).
2. Nath, U., Crawford, B. C. W., Carpenter, R. & Coen, E. Genetic Control of Surface Curvature. *Science (1979)* **299**, 1404–1407 (2003).
3. Armon, S., Bull, M. S., Aranda-Diaz, A. & Prakash, M. Ultrafast epithelial contractions provide insights into contraction speed limits and tissue integrity. *Proceedings of the National Academy of Sciences* **115**, E10333–E10341 (2018).
4. Armon, S., Efrati, E., Kupferman, R. & Sharon, E. Geometry and Mechanics in the Opening of Chiral Seed Pods. *Science (1979)* **333**, 1726–1730 (2011).
5. Guest, S., Kebabze, E. & Pellegrino, S. A zero-stiffness elastic shell structure. *J Mech Mater Struct* **6**, 203–212 (2011).
6. Pezulla, M., Smith, G. P., Nardinocchi, P. & Holmes, D. P. Geometry and mechanics of thin growing bilayers. *Soft Matter* **12**, 4435–4442 (2016).
7. Klein, Y., Efrati, E. & Sharon, E. Shaping of Elastic Sheets by Prescription of Non-Euclidean Metrics. *Science (1979)* **315**, 1116–1120 (2007).
8. McConney, M. E. *et al.* Topography from Topology: Photoinduced Surface Features Generated in Liquid Crystal Polymer Networks. *Advanced Materials* **25**, 5880–5885 (2013).
9. Aharoni, H., Xia, Y., Zhang, X., Kamien, R. D. & Yang, S. Universal inverse design of surfaces with thin nematic elastomer sheets. *Proceedings of the National Academy of Sciences* **115**, 7206–7211 (2018).

10. Kim, J., Hanna, J. A., Byun, M., Santangelo, C. D. & Hayward, R. C. Designing Responsive Buckled Surfaces by Halftone Gel Lithography. *Science (1979)* **335**, 1201–1205 (2012).
11. Wu, Z. L. *et al.* Three-dimensional shape transformations of hydrogel sheets induced by small-scale modulation of internal stresses. *Nat Commun* **4**, 1586 (2013).
12. Nojoomi, A., Jeon, J. & Yum, K. 2D material programming for 3D shaping. *Nat Commun* **12**, 603 (2021).
13. Hajiesmaili, E. & Clarke, D. R. Reconfigurable shape-morphing dielectric elastomers using spatially varying electric fields. *Nat Commun* **10**, 183 (2019).
14. Schild, H. G. Poly(N-isopropylacrylamide): experiment, theory and application. *Prog Polym Sci* **17**, 163–249 (1992).
15. Dong, Y. *et al.* 4D Printed Hydrogels: Fabrication, Materials, and Applications. *Adv Mater Technol* **5**, 2000034 (2020).
16. Hirokawa, Y. & Tanaka, T. Volume phase transition in a nonionic gel. *J Chem Phys* **81**, 6379–6380 (1984).
17. Banerjee, H., Suhail, M. & Ren, H. Hydrogel Actuators and Sensors for Biomedical Soft Robots: Brief Overview with Impending Challenges. *Biomimetics* **3**, 15 (2018).
18. Han, D. *et al.* Soft Robotic Manipulation and Locomotion with a 3D Printed Electroactive Hydrogel. *ACS Appl Mater Interfaces* **10**, 17512–17518 (2018).
19. Larush, L. *et al.* 3D printing of responsive hydrogels for drug-delivery systems. *J 3D Print Med* **1**, 219–229 (2017).
20. Pawar, A. A. *et al.* Rapid Three-Dimensional Printing in Water Using Semiconductor-Metal Hybrid Nanoparticles as Photoinitiators. *Nano Lett* **17**, 4497–4501 (2017).
21. Pawar, A. A. *et al.* High-performance 3D printing of hydrogels by water-dispersible photoinitiator nanoparticles. *Sci Adv* **2**, (2016).
22. Ge, Q. *et al.* 3D printing of highly stretchable hydrogel with diverse UV curable polymers. *Sci Adv* **7**, (2021).
23. Hua, M. *et al.* 4D Printable Tough and Thermoresponsive Hydrogels. *ACS Appl Mater Interfaces* **13**, 12689–12697 (2021).
24. Highley, C. B., Rodell, C. B. & Burdick, J. A. Direct 3D Printing of Shear-Thinning Hydrogels into Self-Healing Hydrogels. *Advanced Materials* **27**, 5075–5079 (2015).
25. Liu, S. & Li, L. Ultrastretchable and Self-Healing Double-Network Hydrogel for 3D Printing and Strain Sensor. *ACS Appl Mater Interfaces* **9**, 26429–26437 (2017).
26. Huang, L. *et al.* Ultrafast Digital Printing toward 4D Shape Changing Materials. *Advanced Materials* **29**, 1605390 (2017).

27. Sydney Gladman, A., Matsumoto, E. A., Nuzzo, R. G., Mahadevan, L. & Lewis, J. A. Biomimetic 4D printing. *Nat Mater* **15**, 413–418 (2016).
28. Zhou, Y., Duque, C. M., Santangelo, C. D. & Hayward, R. C. Biasing Buckling Direction in Shape-Programmable Hydrogel Sheets with Through-Thickness Gradients. *Adv Funct Mater* **29**, 1905273 (2019).
29. Boley, J. W. *et al.* Shape-shifting structured lattices via multimaterial 4D printing. *Proceedings of the National Academy of Sciences* **116**, 20856–20862 (2019).
30. Efrati, E., Sharon, E. & Kupferman, R. Elastic theory of unconstrained non-Euclidean plates. *J Mech Phys Solids* **57**, 762–775 (2009).
31. Klein, Y., Venkataramani, S. & Sharon, E. Experimental Study of Shape Transitions and Energy Scaling in Thin Non-Euclidean Plates. *Phys Rev Lett* **106**, 118303 (2011).
32. Huang, C., Wang, Z., Quinn, D., Suresh, S. & Hsia, K. J. Differential growth and shape formation in plant organs. *Proceedings of the National Academy of Sciences* **115**, 12359–12364 (2018).
33. Sharon, E., Roman, B. & Swinney, H. L. Geometrically driven wrinkling observed in free plastic sheets and leaves. *Phys Rev E* **75**, 046211 (2007).
34. Portet, T. *et al.* Ripples at edges of blooming lilies and torn plastic sheets. *Biophysj* **121**, 2389–2397 (2022).
35. Sawhney, R. & Crane, K. Boundary First Flattening. *ACM Trans Graph* **37**, 1–14 (2018).
36. Panetta, J. *et al.* Computational inverse design of surface-based inflatables. *ACM Trans Graph* **40**, 1–14 (2021).
37. Levin, I. & Sharon, E. Anomalously Soft Non-Euclidean Springs. *Phys Rev Lett* **116**, 035502 (2016).
38. Grossman, D., Sharon, E. & Diamant, H. Elasticity and Fluctuations of Frustrated Nanoribbons. *Phys Rev Lett* **116**, 258105 (2016).
39. Sun, K. & Mao, X. Fractional Excitations in Non-Euclidean Elastic Plates. *Phys Rev Lett* **127**, 98001 (2021).
40. Thérien-Aubin, H., Wu, Z. L., Nie, Z. & Kumacheva, E. Multiple shape transformations of composite hydrogel sheets. *J Am Chem Soc* **135**, 4834–4839 (2013).
41. Timoshenko, S. Analysis of Bi-Metal Thermostats. *J Opt Soc Am* **11**, 233 (1925).

Supplementary information

The reduction of the growth rule to metric and curvature

Introducing a general swelling field, $\omega(z)$, to a voxel-sized, ℓ_0 , will result in the swelling of the midline, ω_0 , and curvature κ . For $-\frac{t}{2} \leq z \leq \frac{t}{2}$ we get that $\bar{\ell}(z) = \ell_0 \omega(z)$ and that $\ell(z) = \omega_0 \ell_0 (1 + \kappa z)$.

The energy, of that voxel, is

$$E(z) \propto \left(\bar{\ell}(z) - \ell(z) \right)^2 \propto \left(\omega(z) - \omega_0 (1 + \kappa z) \right)^2 = \omega^2(z) - 2\omega(z)\omega_0(1 + \kappa z) + \omega_0^2(1 + \kappa z)^2$$

and we minimize $E \equiv \int E(z) dz$, therefore

$$0 = \partial_{\omega_0} E \propto \int dz [-2\omega(z)(1 + \kappa z) + 2\omega_0(1 + \kappa z)^2]$$

hence

$$\int dz \omega(z)(1 + \kappa z) = \int dz \omega_0(1 + \kappa z)^2 = \omega_0 \left(t + \frac{\kappa^2}{12} t^3 \right)$$

Also,

$$0 = \partial_{\kappa} E \propto \int dz [-2\omega(z)\omega_0 z + 2\omega_0^2(z + \kappa z^2)]$$

hence

$$\int dz \omega(z) z = \int dz \omega_0(z + \kappa z^2) = \omega_0 \frac{\kappa}{12} t^3$$

then

$$\int dz \omega(z) = \omega_0 \left(t + \frac{\kappa^2}{12} t^3 \right) - \omega_0 \frac{\kappa^2}{12} t^3 = \omega_0 t$$

And finally

$$\begin{aligned} \omega_0 &= \frac{1}{t} \int dz \omega(z) = \langle \omega \rangle \\ \kappa &= \frac{12}{\omega_0 t^3} \int dz \omega(z) z = \frac{12}{\omega_0 t^2} \langle \omega z \rangle \end{aligned}$$

$$\text{In our case } \omega(z) = \begin{cases} \omega_t & z > 0 \\ \omega_b & z \leq 0 \end{cases} \text{ and so } \begin{cases} \omega_0 = \frac{\omega_t + \omega_b}{2} \\ \kappa = \frac{12}{\omega_0 t^3} \frac{t^2}{8} (\omega_t - \omega_b) = \frac{3}{t} \frac{\omega_t - \omega_b}{\omega_t + \omega_b} \end{cases}$$

The latter coincides with Timoshenko's result of $\kappa = \frac{3\epsilon}{2t}$ (for $\epsilon = \frac{\omega_t - \omega_b}{(\omega_t + \omega_b)/2}$)⁴¹.

Calculating ω_0 and Δ for a spherical cap

We are looking for a metric \bar{a} with an associated Gaussian curvature $\bar{K} \equiv R^{-2}$, where R is the desired radius of the spherical cap. Utilizing the inherent symmetry of the problem, we can work in polar coordinates and assume ω_0 has no azimuthal dependence, hence, $\bar{a} \equiv \omega_0^2(r) \begin{pmatrix} 1 & 0 \\ 0 & r^2 \end{pmatrix}$.

Using Brioschi formula for diagonal metric, $\bar{K} = \frac{r\omega_0'^2 - \omega_0(\omega_0' + r\omega_0'')}{r\omega_0^4}$, solving this differential equation yield $\omega_0(r) = \frac{R c_1 \operatorname{sech}(c_1(\log r + R c_2))}{r}$, where c_1 and c_2 are constants of integration.

To get a cap and to void a sharp cusp at $r \rightarrow 0$ we choose $c_1 = 1$, and continue to determine c_2 such as $\omega_0(r = 0) = 1.25$ (the maximal swelling possible).

Then, the maximal radius of the printed disc is given by $\omega_0(r_{\max}) = 1$ (the minimal swelling possible).